

The thermal and gravitational energy densities in the large-scale structure of the Universe

YI-KUAN CHIANG,¹ RYU MAKIYA,² EIICHIRO KOMATSU,^{3,2} AND BRICE MÉNARD^{4,2}

¹Center for Cosmology and AstroParticle Physics (CCAPP), The Ohio State University, Columbus, OH 43210, USA

²Kavli Institute for the Physics and Mathematics of the Universe (Kavli IPMU, WPI), University of Tokyo, Chiba 277-8582, Japan

³Max-Planck-Institut für Astrophysik, Karl-Schwarzschild Str. 1, 85741 Garching, Germany

⁴Department of Physics & Astronomy, Johns Hopkins University, 3400 N. Charles Street, Baltimore, MD 21218, USA

ABSTRACT

As cosmic structures form, matter density fluctuations collapse gravitationally and baryonic matter is shock-heated and thermalized. We therefore expect a connection between the mean gravitational potential energy density of collapsed halos, Ω_W^{halo} , and the mean thermal energy density of baryons, Ω_{th} . These quantities can be obtained using two fundamentally different estimates: we compute Ω_W^{halo} using the theoretical framework of the halo model which is driven by dark matter statistics, and measure Ω_{th} using the Sunyaev-Zeldovich (SZ) effect which probes the mean thermal pressure of baryons. First, we derive that, at the present time, about 90% of Ω_W^{halo} originates from massive halos with $M > 10^{13} M_{\odot}$. Then, using our measurements of the SZ background, we find that Ω_{th} accounts for about 80% of the kinetic energy of the baryons available for pressure in halos at $z \lesssim 0.5$. This constrains the amount of non-thermal pressure, e.g., due to bulk and turbulent gas motion sourced by mass accretion, to be about $\Omega_{\text{non-th}} \simeq 0.4 \times 10^{-8}$ at $z = 0$.

Keywords: cosmology: miscellaneous — large-scale structure of universe

1. INTRODUCTION

Inspired by the “cosmic energy inventory” program (Fukugita & Peebles 2004), we estimate the cosmic mean densities of two related forms of energies: the thermal (Ω_{th}) and gravitational potential energy (Ω_W) in large-scale structure of the Universe. As structure formation proceeds, the gravitational energy associated with matter density fluctuations is converted into kinetic energy, most of which thermalizes via shocks (Cen & Ostriker 1999; Miniati et al. 2000). Thus, the comparison between Ω_{th} and Ω_W characterizes the efficiency of thermalization in large-scale structure. These quantities, which can be inferred in two fundamentally different ways, provide an important consistency check of the cosmic energy inventory. In addition, precise enough estimates might allow us to constrain the amount of non-thermal energy, disentangle gravitational and non-gravitational heating, and assess the level of virialization of dark matter halos. This is the goal of our analysis.

Early estimates of the amount of thermal energy were introduced in Cen & Ostriker (1999); Refregier et al. (2000); Zhang & Pen (2001); Zhang et al. (2004) using analytical models and cosmological hydrodynamical simulations. Estimates of the amount of gravitational potential energy were presented by Fukugita & Peebles

(2004) which led to the first estimates of Ω_W for dark matter halos but for only two coarse halo mass bins.

It is now timely to revisit these estimates. First, our quantitative understanding of the large-scale structure of the Universe has significantly improved, in terms of the cosmological parameter estimation and, mainly, in terms of the dark matter halo statistics. Second, we now have access to observational constraints on Ω_{th} as a function of redshift, using recent measurements of halo bias-weighted electron pressure of the Universe from the thermal Sunyaev-Zeldovich (SZ) effect (Sunyaev & Zeldovich 1972). This quantity can be constrained by cross-correlating data from the Planck satellite (Planck Collaboration et al. 2016a,b) with galaxies tracing the matter density field (Vikram et al. 2017; Pandey et al. 2019; Koukoufilippas et al. 2020). In particular, our recent work (Chiang et al. 2020, hereafter Paper I) probes this signal over a wider redshift range with better controlling systematic effects due to contamination of the Galactic foregrounds and the cosmic infrared background (CIB) than previous work. We compare these improved estimates of Ω_{th} and Ω_W as a function of the cosmic time, and use them to infer the corresponding amount of non-thermal energy.

In this paper we focus on energy densities associated with the formation of large-scale structure, in the sense

that we do not consider dissipative gravitational settling involved in star formation and accretion disks. The rest of the paper is organized as follows. In Section 2, we review our measurement of Ω_{th} obtained in Paper I. In Section 3, we present our calculations of Ω_W from all large-scale structure of the Universe as well as that from collapsed structures (halos). In Section 4, we solve the Layzer-Irvine equation to find the relationship between the kinetic energy density and Ω_W . We interpret the results and conclude in Section 5.

Throughout, we use the Planck 2018 “TT,TE,EE+lowE+lensing” cosmological parameters given in Table 1 of Planck Collaboration et al. (2020): $(h, \Omega_c h^2, \Omega_b h^2, A_s, n_s) = (0.6737, 0.1198, 0.02233, 2.097 \times 10^{-9}, 0.9652)$, with the minimal mass for neutrinos (0.06 eV). The density parameter of the massive neutrinos is $\Omega_\nu h^2 = 0.06/93.14 = 6.4 \times 10^{-4}$. Thus, the total mass density parameter is $\Omega_m = \Omega_c + \Omega_b + \Omega_\nu = 0.3146$ and the cosmological constant is given by $\Omega_\Lambda = 1 - \Omega_m$. The mean baryon fraction in halos is given by $f_b = \Omega_b/(\Omega_c + \Omega_b) = 0.157$.

2. THERMAL ENERGY DENSITY

The density parameter for the comoving thermal energy density ρ_{th} , which is related to the mean physical thermal pressure $\langle P_{\text{th}} \rangle$, can be defined as¹

$$\Omega_{\text{th}}(z) \equiv \frac{\rho_{\text{th}}(z)}{\rho_{\text{crit}}} = \frac{\langle P_{\text{th}}(z) \rangle}{\rho_{\text{crit}}(1+z)^3}, \quad (1)$$

where $\rho_{\text{crit}} = 1.054 \times 10^4 h^2 \text{ eV cm}^{-3}$ is the present-day critical energy density.

Following Cen & Ostriker (1999) and Refregier et al. (2000), an estimate of this quantity can be obtained by writing the pressure in terms of the gas density-weighted temperature defined by $k_B \bar{T}_\rho \equiv k_B \langle \rho_{\text{gas}} T_{\text{gas}} \rangle / \langle \rho_{\text{gas}} \rangle = \langle P_{\text{gas}} \rangle / \langle n_{\text{gas}} \rangle$ where k_B is the Boltzmann constant, $n_{\text{gas}} = (8 - 5Y)\rho_b / (4m_p)$ with m_p being the proton mass and Y the primordial Helium mass fraction. In this way, one obtains (see Eq. (4) of Zhang et al. 2004)

$$\Omega_{\text{th}}(z) = 1.78 \times 10^{-8} \frac{k_B \bar{T}_\rho(z)}{0.2 \text{ keV}} \frac{\Omega_b}{0.049}. \quad (2)$$

These authors attempted to estimate \bar{T}_ρ using hydrodynamical simulations.

In Paper I we provided a detailed description of Ω_{th} . Assuming that the gas is fully ionized, which is valid for hot gas in galaxy groups and clusters, we can express the

thermal gas pressure P_{th} in terms of that of the electrons by $P_{\text{th}} = (8 - 5Y)/(4 - 2Y) P_e$. For $Y = 0.24$ (Planck Collaboration et al. 2020, the uncertainty (± 0.008) is negligible for our analysis), $P_{\text{th}} = 1.932 P_e$. The mean electron pressure $\langle P_e \rangle$ is the quantity we constrained in Paper I. By measuring the large-scale correlation between tracers of matter overdensities (galaxies and quasars) and the SZ effect, one can constrain the halo bias-weighted electron pressure, $\langle bP_e \rangle(z)$ (Vikram et al. 2017), which is directly proportional to the observable $b_y \times dy/dz$:

$$\langle bP_e \rangle = \langle P_e \rangle b_y = \frac{m_e c^2 (1+z)}{\sigma_T} \frac{dz}{d\chi} \left(b_y \frac{dy}{dz} \right), \quad (3)$$

where σ_T is the Thomson scattering cross section, m_e the electron mass, c the speed of light, χ the comoving radial distance, y the Compton y parameter, and b_y the SZ-weighted halo bias (see below). Inferring $\Omega_{\text{th}}(z)$ thus requires estimating the two key quantities $\langle bP_e \rangle$ and b_y . We present them below.

2.1. Observational constraints from SZ measurements

In Paper I, we estimated $\langle bP_e \rangle(z)$ by measuring angular correlations between the SZ signal and galaxies and quasars tracing the matter density field. To do so, we measured angular two-point cross-correlation functions, $w(\theta, z)$, of intensity maps in microwave bands from the Planck mission (at 100, 143, 217, 353, 545 and 857 GHz; Planck Collaboration et al. 2016a) and the locations of two million spectroscopic galaxies and quasars from the Sloan Digital Sky Survey (SDSS; York et al. 2000) over $0 < z \lesssim 3$. The spectroscopic redshift references include the main, the Baryon Oscillation Spectroscopic Survey, and the Extended Baryon Oscillation Spectroscopic Survey samples (Eisenstein et al. 2001; Strauss et al. 2002; Blanton et al. 2005; Schneider et al. 2010; Reid et al. 2016; Pâris et al. 2017; Ata et al. 2018; Bautista et al. 2018). We also use the reprocessed Infrared Astronomical Satellite (IRAS) data (Miville-Deschênes & Lagache 2005) at 3 and 5 THz for a better separation of the CIB and the SZ effect.

To probe the regime relevant to the large-scale structure formation, we focus on the large-scale limit of the two-point correlation function called the “2-halo term” (Cooray & Sheth 2002). We measured $w(\theta, z)$ integrated over $\theta_{\text{min}}(z) < \theta < \theta_{\text{max}}(z)$. The maximum angular scale is chosen as $\theta_{\text{max}}(z) = 8 \text{ Mpc}/D_A(z)$ where $D_A(z)$ is the proper angular diameter distance, so that the results are not affected by the systematic large-scale zero point fluctuations. The minimum angular scale is chosen as $\theta_{\text{min}}(z) = 3 \text{ Mpc}/D_A(z)$ at 100 and 143 GHz and $2 \text{ Mpc}/D_A(z)$ at higher frequencies, so that the measured cross-correlation is dominated by the 2-halo term

¹ Note that we define the thermal energy density in terms of the thermal pressure. If we defined it in terms of the thermal kinetic energy instead, we should multiply Eq. (1) by 3/2.

(see Figure 3 of Vikram et al. 2017, also see Appendix A of Paper I where we tested the combined effect of this plus non-linear galaxy bias). The larger θ_{\min} for 100 and 143 GHz is due to their larger beam sizes. We determined the best-fitting large-scale amplitudes of the SZ effect by marginalizing over the CIB parameters.

Alternatively, one can use the small-scale limit of the two-point correlation function called the “1-halo term” (via, e.g., stacking analysis equivalent of the cross-correlation function on small angular separations), which is sensitive to the average thermal pressure profile of halos. This measurement can probe the redistribution of thermal energy in halos by baryonic feedback of, e.g., active galactic nuclei (AGN; Planck Collaboration et al. 2013a; Van Waerbeke et al. 2014; Greco et al. 2015; Ruan et al. 2015; Ma et al. 2015; Hojjati et al. 2015, 2017; Crichton et al. 2016; Spacek et al. 2016, 2017; Soergel et al. 2017; Lim et al. 2018a,b; Hall et al. 2019; Tanimura et al. 2020), though the contribution of the 2-halo term should still be taken into account when interpreting the measurement (Hill & Spergel 2014; Battaglia et al. 2015; Hill et al. 2018).

2.2. Thermal pressure bias normalization

We now explain our halo model, which allows us to (i) calculate and correct for b_y from the observed 2-halo term angular correlation to derive the mean pressure $\langle P_e \rangle$, and (ii) interpret the amplitude of $\langle P_e \rangle$ as contributions from halos with the halo mass-pressure normalization quantified by a mass bias parameter.

Following the steps presented in Paper I, we use a model for the 2-halo term (correlation between two halos, see Komatsu & Kitayama 1999) of the angular cross power spectrum. The angular cross-correlation function of the SZ and spectroscopic galaxy data at a given redshift, $w(\theta, z)$, is related to the angular cross power spectrum, $C_\ell(z)$, as $w(\theta, z) = (2\pi)^{-1} \int_0^\infty \ell d\ell C_\ell(z) J_0[(\ell + 1/2)\theta]$, where $J_0(x)$ is the Bessel function of order 0. We model the 2-halo term as (e.g., Makiya et al. 2018)

$$C_\ell^{2h}(z_i) = \int dz' \frac{dV}{dz' d\Omega} f_\ell^y(z') f_\ell^g(z', z_i) P(k_\ell, z'), \quad (4)$$

where $dV/dz d\Omega$ is the comoving volume element per unit solid angle, $k_\ell \equiv (\ell + 1/2)/[(1+z)D_A(z)]$, $P(k, z)$ is the matter power spectrum, and z_i is the mean redshift of the i th bin. The functions f_ℓ^g and f_ℓ^y are given in Eq. (23) of Makiya et al. (2018) and Eq. (5) of Komatsu & Kitayama (1999), respectively.

On scales larger than the size of halos, both f_ℓ^g and f_ℓ^y approach ℓ -independent values. The former becomes $f_\ell^g(z, z_i) = b_g(z) W^g(z, z_i)/\chi^2(z)$, where $b_g(z)$ is a linear galaxy bias parameter, $W^g(z, z_i)$ is the normalized

redshift distribution of galaxies within the i th bin, and $\chi(z) = (1+z)D_A(z)$ is the comoving distance out to redshift z . We constrain f_0^g from the auto galaxy power spectra of SDSS. The latter quantity f_ℓ^y yields a halo bias-weighted electron pressure, $\langle bP_e \rangle$, as

$$f_0^y(z) = \frac{\sigma_T}{m_e c^2} \frac{\langle bP_e \rangle(z)}{(1+z)\chi^2(z)}, \quad (5)$$

where

$$\langle bP_e \rangle(z) \equiv (1+z)^3 \int_{M_{\min}}^{M_{\max}} dM \frac{dn}{dM} b_{\text{lin}} E_T, \quad (6)$$

with

$$E_T(M, z) \equiv 4\pi \int_0^{r_{\max}} r^2 dr P_e(r, M, z) \quad (7)$$

being the thermal energy of electrons per halo as defined by Vikram et al. (2017). Here, dn/dM and b_{lin} are the comoving number density (Tinker et al. 2008) and linear bias (Tinker et al. 2010) of halos, respectively. The halo bias-weighted electron pressure is a direct observable of the SZ-galaxy cross correlation, which requires no assumption about dn/dM or b_{lin} .

To calculate b_y , we follow methodology given in Makiya et al. (2018, 2020).² Its expression is given by

$$b_y(z) = \frac{\int dM (dn/dM) \tilde{y}_0(M, z) b_{\text{lin}}(M, z)}{\int dM (dn/dM) \tilde{y}_0(M, z)}, \quad (8)$$

with $\tilde{y}_0 = \sigma_T E_T / (m_e c^2 D_A^2)$. Here, \tilde{y}_ℓ is the Fourier transform of the 2D profile of the SZ effect within a halo given in Eq. (2) of Komatsu & Seljak (2002). To calculate \tilde{y}_0 we use the universal pressure profile derived from the X-ray and Planck data, which gives $\tilde{y}_0 \propto M^{5/3+\alpha_p}$ with $\alpha_p = 0.12$ (Arnaud et al. 2010; Planck Collaboration et al. 2013b). We may write this as $\tilde{y}_0 \propto GM^{2+\alpha_p}/R$ where $R \propto M^{1/3}$; thus, Eq. (8) can also be seen as gravitational potential energy-weighted halo bias.

The mass M in Eq. (8) is M_{500} , for which the mean overdensity within a halo is 500 times the critical density of the Universe. The dn/dM of Tinker et al. (2008) is given for halo masses defined using various overdensities with respect to the mean mass density of the Universe, $200 \leq \Delta_m \leq 3200$. We thus interpolate the coefficients of dn/dM for an overdensity of $\Delta_m = 500 E^2(z)/[\Omega_m(1+z)^3]$, where $E^2(z) \equiv \Omega_m(1+z)^3 + \Omega_\Lambda$. We then integrate Eq. (8) over M_{500} from $M_{\min} = 10^{11} M_\odot/h$ to $M_{\max} = 5 \times 10^{15} M_\odot/h$.

² Codes are available in <https://github.com/ryumakiya/pysz>.

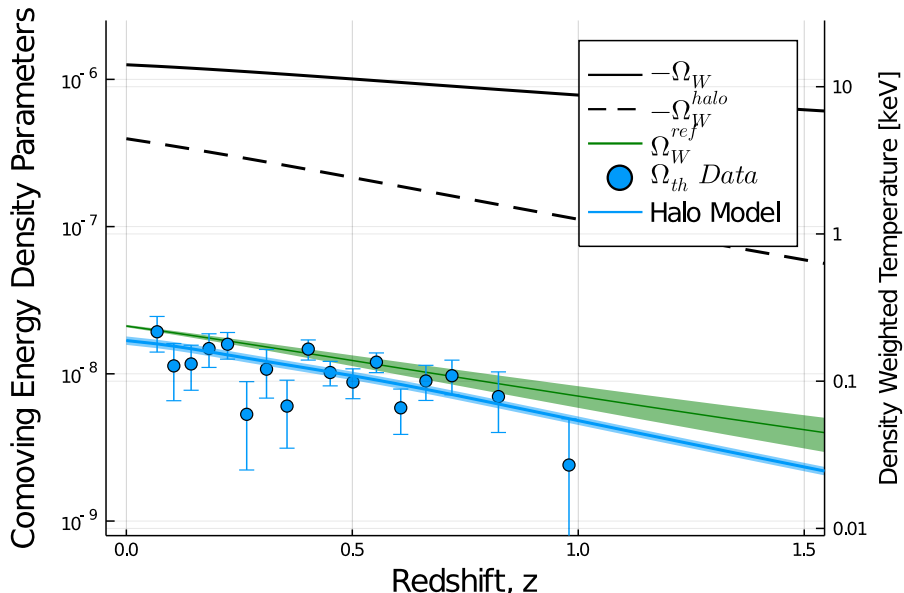


Figure 1. Comoving density parameters of the thermal energy (data points with error bars from Paper I), gravitational potential energy of all large-scale structure of the Universe (black solid line), and that of halos (black dashed line). The lower boundary of the green shaded area shows the halo contribution times the mean baryon fraction $f_b = 0.157$, whereas the upper boundary shows the difference between the corresponding non-linear and linear $P(k)$ contributions. The blue shaded area shows the best-fitting model for Ω_{th} (Eqs. (1, 6, 7, 8)) with a constant mass bias parameter and its 68% confidence level, $B = 1.27^{+0.05}_{-0.04}$. The right axis shows the corresponding values of \bar{T}_ρ for Ω_{th} given in Eq. (2).

Lowering M_{min} to $10^{10} M_\odot/h$ changes ρ_{th} by less than 1, 3, and 10 percent at $z < 1, 2,$ and $3,$ respectively. These changes are smaller than the theoretical uncertainty of dn/dM in the corresponding redshift ranges.

To capture all the thermal pressure associated with a halo, we integrate the pressure profile out to $r_{\text{max}} = 6 r_{500}$, where r_{500} is the radius that encloses $M_{500} = (4\pi/3) E^2(z) \rho_{\text{crit}} r_{500}^3$. This radius approximates the so-called shock radius, beyond which pressure falls rapidly (Bryan & Norman 1998; Lau et al. 2015; Shi 2016; Zhang et al. 2020). For $r_{\text{max}} = 4 r_{500}$ and $8 r_{500}$, we find 0.929 and 1.036 times ρ_{th} for $r_{\text{max}} = 6 r_{500}$, which change the inferred values of the mass bias parameter B , which affects the normalization of the mass-pressure relationship (see below), by 4 and 2 percent, respectively.

Combining our measurements of $\langle bP_e \rangle$ and the estimation of b_y , we obtain estimates of $\Omega_{\text{th}}(z)$, shown with the data points in Figure 1. In particular, we find

$$\Omega_{\text{th}} = (1.7 \pm 0.1) \times 10^{-8} \quad \text{at } z = 0, \quad (9)$$

from the best-fitting model with the 68% confidence level. The best estimate and uncertainty here were derived assuming a constant mass bias parameter B using the posterior reported in Paper I. If we allow for a redshift-dependent B , we find $\Omega_{\text{th}} = (1.5 \pm 0.3) \times 10^{-8}$ at $z = 0$. As there is no evidence for the evolution of B within the redshift range discussed here, we use the

redshift-independent value as the baseline in this paper. Since we measure $\langle bP_e \rangle$ directly over $0 \lesssim z \lesssim 1$, and the estimate of b_y does not depend on the mass bias B , our Ω_{th} estimates within this redshift range should be considered empirical. We have checked the accuracy of the analytical model for b_y using the Magneticum simulation (Dolag et al. 2016) and found that the uncertainty is negligible compared with the statistical uncertainty of Ω_{th} .

To interpret the observed Ω_{th} as the sum of halo contributions with the mass-pressure calibration not precisely known, we parameterize this uncertainty using the so-called ‘‘mass bias parameter’’ B . It relates the true M_{500} of halos to the mass calibrated by X-ray observations (Arnaud et al. 2010) used by the Planck team (Planck Collaboration et al. 2013b) as $B = M_{500}^{\text{true}}/M_{500}^{\text{Planck}}$. It is found that $B > 1$ is required to fit statistics of the Planck SZ data such as number counts and auto- and cross-power spectra (Planck Collaboration et al. 2014, 2016c; Dolag et al. 2016; Hurier & Lacasa 2017; Salvati et al. 2018, 2019; Bolliet et al. 2018, 2020; Makiya et al. 2018, 2020; Osato et al. 2018, 2020; Koukoufilippas et al. 2020). This parameter is related to the commonly used parameter b as $1 - b = B^{-1}$ (see also Horowitz & Seljak 2017, for yet another parameterization). Assuming a mass- and redshift-independent B , which is sup-

ported by the current measurements (Makiya et al. 2018; Salvati et al. 2019; Koukoufilippas et al. 2020; Chiang et al. 2020), we find $B = 1.27_{-0.04}^{+0.05}$ from our measurement of $\langle bP_e \rangle$ (Paper I). The B dependence is simple: $\Omega_{\text{th}} \propto \langle bP_e \rangle \propto B^{-5/3-\alpha_p}$ with $\alpha_p = 0.12$, as the total electron pressure is proportional to $M^{5/3+\alpha_p}$ (Arnaud et al. 2010) with $M = M_{500}^{\text{Planck}} = M_{500}^{\text{true}}/B$.

The physical origin of B is not fully understood. The origin of $B > 1$ is partly due to the presence of non-thermal gas pressure in galaxy clusters, which leads to underestimation of X-ray calibrated mass assuming hydrostatic equilibrium between gravity and thermal gas pressure gradient (Kay et al. 2004; Rasia et al. 2006, 2012; Nagai et al. 2007; Jeltema et al. 2008; Piffaretti & Valdarnini 2008; Lau et al. 2009; Meneghetti et al. 2010; Nelson et al. 2012, 2014b; Shi & Komatsu 2014; Shi et al. 2016; Biffi et al. 2016; Henson et al. 2017; Vazza et al. 2018; Angelinelli et al. 2020; Ansarifard et al. 2020). It is possible that some of $B > 1$ is due to the choice of particular X-ray cluster samples and analysis methods used in Arnaud et al. (2010) and/or Planck Collaboration et al. (2013b). We therefore choose to call this parameter simply ‘‘mass bias’’, without reference to the assumption of hydrostatic equilibrium.

3. GRAVITATIONAL POTENTIAL ENERGY DENSITY

We now estimate the density parameter for the gravitational potential energy as

$$\Omega_W = \frac{\Omega_m}{c^2} W, \quad (10)$$

where W is the gravitational potential energy per unit mass. Considering a system of mass M consisting of particles with mass m_i , such that $M = \sum_i m_i$, we can express its gravitational potential energy as (Section 24 of Peebles 1980)

$$\begin{aligned} MW &= -\frac{1}{2}a^3\rho_m(a) \int d^3x \delta(\mathbf{x}, a)\phi(\mathbf{x}, a) \\ &= -\frac{1}{2}Ga^5\rho_m^2(a) \int d^3x \int d^3x' \frac{\delta(\mathbf{x}, a)\delta(\mathbf{x}', a)}{|\mathbf{x} - \mathbf{x}'|}, \end{aligned} \quad (11)$$

where $a(t) = (1+z)^{-1}$ is the scale factor, \mathbf{x} denotes the comoving coordinates, $\delta(\mathbf{x}, a)$ is the matter density contrast, and $\phi(\mathbf{x}, a)$ is the peculiar gravitational potential. The factor 1/2 corrects double-counting of particles contributing to both δ and ϕ .

For a uniform density sphere with a physical radius R_p , an excess mass above the mean $\delta M = (4\pi/3)\delta\rho_m R_p^3$, and a potential $\phi(r_p \leq R_p) = -2\pi G\delta\rho_m(R_p^2 - r_p^2/3)$, we find $MW = -3G(\delta M)^2/(5R_p)$, which agrees with the known result for gravitational potential energy of a uniform density sphere.

Going to Fourier space and taking ensemble average of Eq. (11), we obtain

$$MW = -\frac{1}{2}\rho_{m0} \left(\int d^3x \right) \int \frac{d^3k}{(2\pi)^3} P_{\phi\delta}(k, a), \quad (12)$$

where $\rho_{m0} = \rho_m a^3$ is the present-day mean mass density. The cross-correlation power spectrum of ϕ and δ , $P_{\phi\delta}(k)$, is related to the matter density power spectrum $P(k)$ via the Poisson equation:

$$P_{\phi\delta}(k, a) = -4\pi G \frac{\rho_{m0}}{a} \frac{P(k, a)}{k^2}. \quad (13)$$

Dividing both sides of Eq. (12) by $M = \rho_{m0} \int d^3x$, we obtain the gravitational potential energy per unit mass of large-scale structure of the Universe. Using the Friedmann equation, $H_0^2 = (8\pi G/3)\rho_{\text{crit}}$, and $\rho_{m0} = \Omega_m \rho_{\text{crit}}$, we find

$$W = -\frac{3\Omega_m H_0^2}{8\pi^2 a} \int_0^\infty dk P(k, a). \quad (14)$$

Multiplying this by $\Omega_m/2$ agrees with Eq. (60) of Fukugita & Peebles (2004) for the binding energy for the present-day epoch with $a = 1$.

The gravitational potential energy W per unit mass, or equivalently, the density parameter Ω_W , is *exactly* given by the integral over the matter power spectrum $P(k)$. It does not rely on any assumption and is valid irrespective of other aspects of the density field, such as non-Gaussian or higher-order statistical properties.

When we calculate W from all forms of matter in the Universe, we use ρ_{m0} and $P(k)$ including baryons, cold dark matter (CDM), and neutrinos. When we calculate W from halos in the next section, we exclude the contribution from neutrinos as they cluster on halo scales only weakly. This simple prescription has been shown to work well for the halo mass function (Ichiki & Takada 2012; Costanzi et al. 2013), bias and power spectrum (Villaescusa-Navarro et al. 2014; Castorina et al. 2014), and statistics of the SZ effect (Bolliet et al. 2020). Thus, for halo-based calculations, we replace ρ_{m0} with $\rho_{\text{cb0}} \equiv \rho_{\text{b0}} + \rho_{\text{c0}}$, and use the baryon+CDM power spectrum, $P_{\text{cb}}(k)$, to compute all the necessary ingredients of the halo model.

3.1. Contribution from halos

The total gravitational potential energy density in the Universe includes contributions from all large-scale structures, which can be evaluated using the non-linear matter $P(k)$ in Eq. (14). In contrast, as shown in Paper I, the total thermal energy density in the Universe is dominated by collapsed halos, especially massive clusters and groups. To meaningfully compare the two,

we need to estimate the contribution of Ω_W originating from halos.

To this end, we use the halo model (Cooray & Sheth 2002) to write $P(k) = P_{1h}(k) + P_{2h}(k)$, where P_{1h} and P_{2h} are the 1- and 2-halo terms, respectively. In this section we focus on the 1-halo term, to extract Ω_W originating from halos. The 1-halo term is given by (Seljak 2000)

$$P_{1h}(k, a) = \frac{1}{\rho_{cb0}^2} \int_{M_{\min}}^{M_{\max}} dM \frac{dn}{dM} M^2 |u(kR, c)|^2, \quad (15)$$

where $u(x, c)$ is the Fourier transform of the halo mass density profile to be specified, normalized such that $u(x) \rightarrow 1$ for $x \rightarrow 0$, and c is the concentration parameter³. Here, R is the characteristic comoving radius of a halo, e.g., the comoving virial radius. It is related to the mass enclosed within R as $M = (4\pi/3)\rho_{cb0}\Delta_m R^3$, where Δ_m is the overdensity of a halo with respect to the mean mass density of the Universe. We use a comoving radius rather than a physical one, as k in the power spectrum is the comoving wavenumber.

Using $P_{1h}(k)$ in Eq. (14), we obtain

$$W_{1h} = -\frac{1}{\pi a} \frac{1}{\rho_{cb0}} \int dM \frac{dn}{dM} \frac{GM^2}{R} \int_0^\infty dx |u(x, c)|^2. \quad (16)$$

We may use the physical radius, $R_p = aR$, to re-write this result as

$$W_{1h} = -\frac{1}{\rho_{cb0}} \int_{M_{\min}}^{M_{\max}} dM \frac{dn}{dM} \frac{GM^2}{R_p} A_g(c), \quad (17)$$

where

$$A_g(c) \equiv \int_0^\infty \frac{dx}{\pi} |u(x, c)|^2. \quad (18)$$

Eq. (17) has a clear physical meaning. The Fourier transform of the density profile of a uniform density sphere is $u(x) = 3j_1(x)/x$, where $j_1(x) = [\sin(x) - x \cos(x)]/x^2$ is the spherical Bessel function of order 1 and $x = kR$. Integrating over x , we obtain $A_g = 3/5$. Thus, $-A_g GM^2/R_p = -3GM^2/(5R_p)$ agrees with the gravitational potential energy of a uniform density sphere with a physical radius R_p . Therefore, W_{1h} is the mean gravitational potential energy density of halos per unit mass. The contribution as a function of halo mass is shown in Figure 2 (dotted lines) at $z = 0$ and 1.

³ Here, $u(x, c)$ is the total mass density profile and we do not yet distinguish between the density profiles of dark matter and baryons. Later we adopt a Navarro-Frenk-White (NFW) profile (Navarro et al. 1996, 1997) for $u(x, c)$, which is a good approximation to the dark matter density profile. On the other hand the baryonic matter distribution is less concentrated than the dark matter (Schaan et al. 2020). We comment on this uncertainty in Section 3.3.

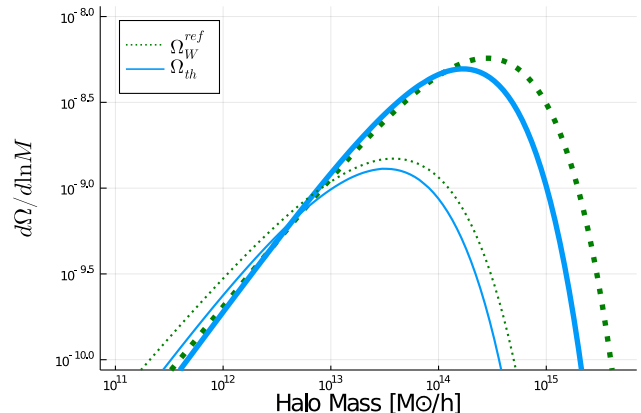


Figure 2. Contribution to $\Omega_W^{\text{ref}} = -f_b \Omega_W^{\text{halo}}/3$ (Eq. (23); dotted lines) and Ω_{th} (solid lines) per logarithmic mass interval, at $z = 0$ (thick lines) and 1 (thin lines). The mass for Ω_W^{halo} is computed with $\Delta_m = 200$, while Ω_{th} is with M_{500} .

Figure 2 also shows that the thermal energy density has a similar mass scaling, as

$$\Omega_{\text{th}} \propto \int dM \frac{dn}{dM} E_T \propto \int dM \frac{dn}{dM} \frac{GM^{2+\alpha_p}}{R_p}, \quad (19)$$

where E_T is the thermal energy of electrons per halo defined in Eq. (7) and $\alpha_p = 0.12$. The contributions to Ω_W^{halo} and Ω_{th} per logarithmic mass interval differ only slightly due to the small departure from the self-similar behavior quantified by α_p and the different mass definitions used (M_{200m} for Ω_W^{halo} and M_{500} for Ω_{th}).

3.2. Numerical results

To evaluate Eq. (14), we use three power spectra:⁴ (1) the linear matter power spectrum from the public Boltzmann solver CLASS (Blas et al. 2011), (2) the non-linear matter power spectrum from “Halofit” (Smith et al. 2003) with the parameters updated by Takahashi et al. (2012), and (3) the 1-halo term, $P_{1h}(k)$. For (1) and (2) we use $P(k)$ including baryons, CDM, and neutrinos. For (3) we exclude the contribution from neutrinos.

For dn/dM we use Tinker et al. (2008) with $\Delta_m = 200$. For the halo density profile, we use an NFW profile (Navarro et al. 1996, 1997). For this profile we use the analytical result for Fourier transform given in Scoccimarro et al. (2001) and integrate Eq. (18) to obtain $A_g(c)$. To obtain this analytical Fourier transform, they assume that the halo density profile is truncated at $R = cr_s$ where r_s is a comoving NFW scale radius. In our setup, $R = R_{200m}$ within which the mean overdensity of

⁴ Julia codes are available in <https://github.com/komatsu5147/OmegaGrav.jl>.

a halo is $\Delta_m = 200$ times the mean mass density of the Universe.

This treatment adds a subtlety: what if we truncate the density profile at a larger radius? W_{1h} would increase. At the same time, such halo outskirts may not be virialized completely; thus, it is not clear how to count the contribution in this region. For this reason we regard W_{1h} computed here as a lower bound for the mean gravitational potential energy of halos per unit mass. An upper bound comes from the difference between the non-linear and linear $P(k)$ contributions, which can be computed without ambiguity about the halo boundary.

We find a convenient fitting formula for $A_g(c) \simeq 1.0202 + \sum_{i=1}^4 a_i (c - 5)^i$ with $a_i = 5.376 \times 10^{-2}$, -1.842×10^{-3} , 9.489×10^{-5} , and -2.352×10^{-6} for $i = 1, 2, 3$, and 4 , respectively. This formula is accurate to better than 0.1 percent everywhere in $2 \leq c \leq 20$.

For $c(M, z)$ we use the formula given in [Duffy et al. \(2008\)](#) for $\Delta_m = 200$: $c(M, z) = 10.14 (M/2 \times 10^{12} M_\odot/h)^{-0.081} (1+z)^{-1.01}$. Thus, $A(c)$ is greater than $3/5$, which means that an NFW halo is more tightly bound than a uniform density sphere. For the mass integral in Eq. (15), we use the same M_{\min} and M_{\max} as in Section 2.

We integrate $\int dk P(k)$ from $k = 5 \times 10^{-4}$ to $30 h \text{ Mpc}^{-1}$, in which the halofit model is calibrated against the simulation. Extending to $k_{\max} = 100 h \text{ Mpc}^{-1}$ increases the result for non-linear $P(k)$ only by 0.5 percent at $z = 0$ and less at higher redshifts and for linear $P(k)$.

In Figure 1 we show our estimate of Ω_W for the non-linear $P(k)$ (solid line) and 1-halo $P(k)$ (dashed line). We find

$$\frac{\Omega_W^{\text{halo}}}{\Omega_W^{\text{tot}}} \simeq 0.3 \text{ at } z = 0. \quad (20)$$

This implies that, at the present time, there is substantially more potential energy in the large-scale structure (or 2-halo component) than that in gravitationally bound halos (the 1-halo component). The numerical values are given in Table 1. The 1-halo term's contribution is 30 percent that of the non-linear $P(k)$ at $z = 0$, and declines to 15 percent at $z = 1$. The 5, 6 and 7th columns show the halo contributions from $M > 10^{12}$, 10^{13} , and $10^{14} M_\odot/h$. We find that most of the contributions to Ω_W^{halo} come from massive halos: 65 and 90 percent from $M > 10^{14}$ and $10^{13} M_\odot/h$ at $z = 0$, respectively, and 70 percent from $M > 10^{13} M_\odot/h$ at $z = 1$.

The 1-halo contribution integrated up to $R = R_{200m}$ agrees well with the difference between the non-linear and linear $P(k)$ contributions at $z = 0$, while it is somewhat smaller at higher redshifts. The lower boundary of

the green shaded area shows the 1-halo $P(k)$ times $2/3$ the mean baryon fraction, whereas the upper boundary shows the difference between the non-linear and linear $P(k)$ contributions times $2/3$ the mean baryon fraction. The green shaded area in Figure 1 therefore shows the lower and upper bounds for a contribution in potentially non-virialized regions of halo outskirts.

3.3. Accuracy and uncertainty

[Fukugita & Peebles \(2004\)](#) previously provided an order-of-magnitude estimate of the gravitational potential energy in large-scale structure using the non-linear $P(k)$ estimate available at the time. Thanks to an improved understanding of non-linear matter clustering and precision determination of the cosmological parameters today, we can now estimate Ω_W with greater accuracy and the meaningful error estimates.

The dominant uncertainty for Ω_W from the linear $P(k)$ is the primordial scalar amplitude parameter A_s , which is known to better than 2 percent precision ([Planck Collaboration et al. 2020](#)). Uncertainty for Ω_W from the non-linear $P(k)$ is larger than this because accuracy of the halofit $P(k)$ at $k > 1 h \text{ Mpc}^{-1}$ is at the level of 5–10 percent depending on the wavenumber ([Takahashi et al. 2012](#)). We thus quote 7 percent uncertainty for Ω_W from the non-linear $P(k)$ at $z \leq 1.5$. The uncertainty at higher z is smaller due to smaller non-linearity.

[Fukugita & Peebles \(2004\)](#) gave rough estimates of Ω_W^{halo} for halos of typical L^* galaxies and clusters of galaxies. Our calculation of the halo contribution to Ω_W^{halo} based on the 1-halo $P(k)$ term includes contributions from halos of all masses. The accuracy of this calculation is limited by the uncertainties of dn/dM . The precision of dn/dM at $z = 0$ is 5 percent ([Tinker et al. 2008](#)). The uncertainty increases for larger redshifts because the time dependence of dn/dM is still not understood very well. We thus quote 10 percent uncertainty for Ω_W^{halo} at $z = 1.5$. Nonetheless, we find that Ω_W computed with dn/dM from [Tinker et al. \(2008\)](#) and [Tinker et al. \(2010\)](#) agree to within 2 percent at $z \leq 1.5$, if the halo multiplicity function of [Tinker et al. \(2010\)](#) is re-normalized to unity at each z .

Other sources of uncertainty include the effect of baryonic feedback on the matter power spectrum ([van Daalen et al. 2011](#)), halo profile ([Gnedin et al. 2004](#)), and dn/dM ([Bocquet et al. 2016](#)). The uncertainty due to these effects is comparable to the current uncertainty for our calculations of Ω_W from the non-linear $P(k)$ and halos. We thus add the uncertainties in quadrature.

To summarize, the uncertainties in Ω_W from the linear and non-linear $P(k)$ are 2 and 10 percent, respectively,

Table 1. The density parameters of the gravitational potential energy (Eq. (10)), Ω_W , for the linear (Ω_W^{lin}), non-linear (Ω_W^{nl}), and 1-halo $P(k)$ (Ω_W^{halo}). The 1st column shows the redshift z , while the 2nd, 3rd and 4th columns show $-10^7\Omega_W^{\text{lin}}/2$, $-10^7\Omega_W^{\text{nl}}/2$ and $-10^7\Omega_W^{\text{halo}}/2$, respectively. The 5th, 6th and 7th columns show $-10^7\Omega_W^{\text{halo}}/2$ from halos with the mass $M > 10^{12}$, 10^{13} and $10^{14} M_\odot/h$, while the 8th and 9th columns show $-10^8 f_b \Omega_W^{\text{halo}}/3$ and $-10^8 f_b (\Omega_W^{\text{nl}} - \Omega_W^{\text{halo}})/3$, respectively. See Section 3.3 for the modelling uncertainties in Ω_W^{lin} (2 percent for all z), Ω_W^{nl} (10 percent for all z), and Ω_W^{halo} (7 to 14 percent from $z = 0$ to 1.5). The redshift points are chosen to allow for the precise interpolation between them.

z	$-10^7\Omega_W^{\text{lin}}/2$	$-10^7\Omega_W^{\text{nl}}/2$	$-10^7\Omega_W^{\text{halo}}/2$	$> 10^{12}$	$> 10^{13}$	$> 10^{14} M_\odot/h$	$-10^8 f_b \Omega_W^{\text{halo}}/3$	$-10^8 f_b (\Omega_W^{\text{nl}} - \Omega_W^{\text{lin}})/3$
0.0	4.23	6.28	1.98	1.96	1.84	1.26	2.07	2.15
0.3	4.00	5.55	1.39	1.37	1.23	0.68	1.46	1.62
0.5	3.76	5.03	1.08	1.05	0.91	0.41	1.13	1.34
0.7	3.50	4.54	0.83	0.80	0.65	0.24	0.87	1.10
1.0	3.12	3.91	0.56	0.53	0.39	0.089	0.59	0.82
1.3	2.80	3.39	0.38	0.35	0.22	0.029	0.40	0.62
1.5	2.61	3.11	0.30	0.26	0.15	0.013	0.31	0.52

at all z , whereas that from the halos increases from 7 to 14 percent at $z = 0$ to 1.5.

4. THERMAL AND GRAVITATIONAL POTENTIAL ENERGIES

4.1. Virial relation for halos

One can relate the kinetic energy of the gas to the gravitational potential energy, which is dominated by collisionless dark matter particles. For virialized structures such as halos, we can use the virial theorem,

$$K = -\frac{W}{2}. \quad (21)$$

where K is the mean kinetic energy per unit mass, $K = \sum_i m_i v_i^2 / (2 \sum_i m_i)$.

Without depending on the validity of the virial theorem, the kinetic energy term K provides pressure support in halos, and can be separated into thermal and non-thermal components:

$$\rho K = \frac{3}{2} P = \frac{3}{2} (n k_B T + P_{\text{non-th}}), \quad (22)$$

where the relevant non-thermal motion is assumed to be isotropic on the halo scale, thus 2/3 of the non-thermal (kinetic) energy contributes to pressure.

We now introduce the reference potential energy for halos:

$$\Omega_W^{\text{ref}} = -\frac{1}{3} f_b \Omega_W^{\text{halo}}, \quad (23)$$

which corresponds to (minus) the amount of potential energy in halos contributing to the pressure. Here we have assumed that baryons and dark matter share the same kinetic energy per unit mass, therefore a baryon fraction f_b is needed in this expression. This may not

be exact, as baryons and dark matter reach an equilibrium configuration in different ways. The former reaches equilibrium via collisions, whereas the latter is collisionless and thus achieves an equilibrium (virialized) state via exchange of energy between particles and time-dependent gravitational potential (violent relaxation, Lynden-Bell 1967; White 1996). In addition, not all baryons remain in a hot gas phase, but some cool and form stars, making $f_{\text{gas}} < f_b$ (Bryan 2000). While the gas fraction depends on halo mass, for the relevant cluster halos with $M_{500} > 10^{14} M_\odot$, $f_{\text{gas}}/f_b \sim 90\text{--}95\%$ (e.g., Gonzalez et al. 2013). We thus adopt $f_{\text{gas}}/f_b = 0.925 \pm 0.025$ and discuss the impact of this in the following estimate.

Based on the assumptions used in this section, we can quantify the efficiency of gravitational to thermal energy conversion through the ratio

$$\frac{\Omega_{\text{th}}}{\Omega_W^{\text{ref}}} = \frac{1.7 \pm 0.1}{2.07 \pm 0.14} = 0.82 \pm 0.07 \quad \text{at } z = 0. \quad (24)$$

Our estimate indicates that, at the present time, the thermal energy accounts for about 80% of the available reference gravitational energy. The redshift dependence of this ratio is shown in Figure 3. When correcting for $f_{\text{gas}}/f_b = 0.925 \pm 0.025$, the ratio becomes 0.89 ± 0.08 .

If we use the upper bound on the halo contribution (the upper boundary of the green shaded area in Figure 1), i.e., if we replace Ω_W^{halo} by the difference between the non-linear and line power spectra, we find $\Omega_{\text{th}}/\Omega_W^{\text{ref}} \simeq 0.75$ (0.81 when including $f_{\text{gas}}/f_b = 0.925$) for $0 < z \leq 0.5$ and 0.63 (0.68) for $0.5 < z \leq 1$.

We also find that, at $z < 1$, this ratio is approximately 1.3 for the model with no mass bias, i.e. $B = 1$. As B is an empirical parameter for an empirical pressure profile model, $B = 1$ does not represent a physical model

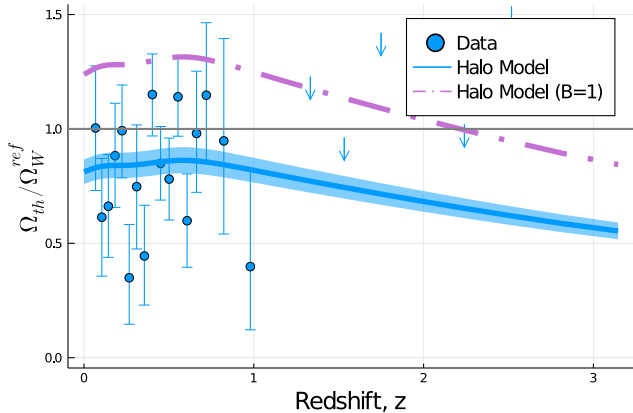


Figure 3. Efficiency of gravitational to thermal energy conversion given by the ratio of the thermal energy density Ω_{th} and the amount of potential energy in halos contributing to the pressure Ω_W^{ref} . The data points with error bars and upper limits shown by the arrows are obtained by dividing the Ω_{th} data shown in Figure 1 by the best-fitting model for Ω_W^{ref} given in Eq. (23). The model uncertainty is not included in the error bars. The shaded area shows the best-fitting model with the 68% confidence level (the halo model for Ω_{th} shown in Figure 1 divided by the best-fitting model for Ω_W^{ref} .) The dashed line shows the (non-physical) ratio for the model with no mass bias, $B = 1$.

in which the total pressure gradient balances gravity of an NFW profile, such as given in Komatsu & Seljak (2001). Therefore, the $B = 1$ model is not guaranteed to give $\Omega_{\text{th}}/\Omega_W^{\text{ref}} \leq 1$. Our approach could be used to put a lower limit on B so that this ratio does not exceed unity.

Finally, we can quantify the non-thermal contribution to the total energy density. Expressing $P_{\text{non-th}}$ given in Eq (22) in terms of the density parameter of non-thermal pressure $\Omega_{\text{non-th}} \equiv \Omega_W^{\text{ref}} - \Omega_{\text{th}}$, we get

$$\Omega_{\text{non-th}} = (0.37 \pm 0.17) \times 10^{-8} \quad \text{at } z = 0. \quad (25)$$

4.2. Comparison to the previous work

In Zhang & Pen (2001), the authors relate the gas temperature to the peculiar gravitational potential as $k_B T_{\text{gas}} = -[4m_p/(8 - 5Y)](\phi - \bar{\phi})/6$, where $\bar{\phi}(\mathbf{x}) = \int d^3x' \phi(\mathbf{x}') W(|\mathbf{x} - \mathbf{x}'|)$ is a high-pass filtered potential. The gas density-weighted temperature, \bar{T}_ρ , is then given by the cross-correlation power spectrum of gas density and ϕ . Using their Eq. (6) in our Eq. (2), we find

$$\Omega_{\text{th}}^{\text{ZP01}} = f_b \frac{\Omega_m^2 H_0^2}{8\pi^2 a} \int_0^\infty dk P_{\text{dg}}(k) [1 - W(k)]. \quad (26)$$

The coefficient agrees with that of our Ω_W^{ref} . Here, $P_{\text{dg}}(k)$ is the cross-correlation power spectrum of dark matter and gas, and $W(k) = \exp(-k^2 r_e^2/2)$ is the Fourier transform of the high-pass filter with a free parameter r_e . The

factor $1 - W(k)$ acts to extract the small-scale contribution, which is dominated by the 1-halo term. Thus, their expression approximates Ω_W^{ref} . Our approach does not require r_e because we isolate the halo contribution using the 1-halo term or the difference between the linear and non-linear $P(k)$.

The dark matter-gas cross-correlation power spectrum takes into account the difference in the spatial distribution of dark matter and gas on small scales. As the distribution of gas is smoother than that of dark matter on small scales, they write $P_{\text{dg}}(k) = \exp(-k^2 r_g^2/2)P(k)$ with another free parameter $r_g \sim 1/3 \text{ Mpc}/h$. This acts to reduce Ω_W^{ref} . We did not include this effect in our calculation, as this is subject to the effect of feedback by supernova explosion and AGN which are not well understood. This is included in the error budget we discussed at the end of Section 3.3.

4.3. Beyond virial theorem for the large-scale structure

The virial relation, $K = -W/2$, does not hold for all the large-scale structure of the Universe. Here we need to take into account the fact that the systems of interest are not isolated and matter keeps accreting.

The evolution of the kinetic and gravitational potential energies of collisionless non-relativistic particles is given by the Layzer-Irvine equation (Layzer 1963; Irvine 1961; Dmitriev & Zeldovich 1964)

$$\frac{d}{dt}(K + W) + \frac{\dot{a}}{a}(2K + W) = 0, \quad (27)$$

where the dot denotes the time derivative. The virial relation is the stationary solution of this equation.

For linear theory (see Eq. (12) of Davis et al. 1997),

$$K = -\frac{2f^2}{3\Omega_m(a)}W, \quad (28)$$

where $f \equiv d \ln \delta_1 / d \ln a$ with the linear density contrast δ_1 and $\Omega_m(a) = \Omega_m/[a^3 E^2(a)]$ is the matter density parameter at a given a . For the virial relation to hold, we need $f = \sqrt{3\Omega_m/4}$ which is not satisfied in general. The dotted lines in Figure 4 show the evolution of the comoving energy density parameters for K (upper) and $-W/2$ (lower) computed from the linear $P(k)$. At $z = 0$ the former is larger than the latter by a factor of 1.17.

To obtain K for the non-linear $P(k)$, we solve the Layzer-Irvine equation numerically. We use the linear solution during the matter-dominated era, $K = -2W/3$, to set the initial condition. The solid lines in Figure 4 show the resulting comoving energy density parameters.

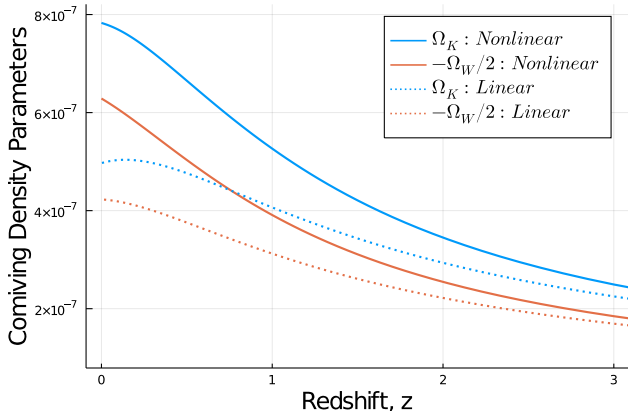


Figure 4. Solutions of the Layzer-Irvine equation (27). We show the comoving energy density parameters of K (Ω_K) and $-W/2$ ($-\Omega_W/2$). The horizontal axis shows the redshift, z . The solid and dotted lines show Ω_K (blue) and Ω_W (orange) for the non-linear and linear $P(k)$, respectively.

At $z = 0$ K is larger than $-W/2$ by a factor of 1.25.⁵ Thus, more kinetic energy is available in large-scale structure of the Universe than that of the stationary solution. This is due to the continuous infall of matter.

The numerical values of the density parameter for the kinetic energy, Ω_K , are given in Table 2. These values should be compared with those in Table 1. This enhanced kinetic energy is associated with bulk flows of matter falling into the gravitational potential. During this stage, the gas carried with it has not yet thermalized with the surrounding hot gas. It is therefore not expected to contribute or perturb the global SZ signal, which is dominated by halo contributions. The solutions of the Layzer-Irvine equation found in this section are therefore not to be compared directly with Ω_{th} , but can be compared with the sum of the thermal SZ effect and, e.g., the kinetic SZ effect probing the bulk momentum density field.

5. DISCUSSION AND CONCLUSION

We have presented estimates of the thermal energy density of baryons Ω_{th} and the gravitational potential energy in collapsed halos Ω_W^{halo} . These quantities are related as the growth of structure leads to a conversion of gravitational energy associated with matter density

⁵ One may wonder if we can use $W_{1h}(a)$ in Eq. (27) and solve for $K_{1h}(a)$. If we did this, we would find $K_{1h} > -W_{1h}/2$ by more than 40 percent despite that halos are virialized. However, this is not correct. Suppose that we split W as $W = W_{1h} + W_{\text{other}}$. While Eq. (27) is satisfied for the sum $W_{1h} + W_{\text{other}}$, it is not satisfied for each component separately. Therefore, we only report Ω_K for the linear and non-linear $P(k)$. The linear $P(k)$ result is only an approximation and for comparison to the non-linear one.

Table 2. The density parameters of the kinetic energy in the large-scale structure of the Universe, Ω_K , for the linear (Ω_K^{lin}) and non-linear $P(k)$ (Ω_K^{nl}). The 1st column shows the redshift z , while the 2nd and 3rd columns show $10^7\Omega_K^{\text{lin}}$ and $10^7\Omega_K^{\text{nl}}$, respectively. The modelling uncertainties in Ω_K are equal to those in the corresponding Ω_W reported in Section 3.3.

z	$10^7\Omega_K^{\text{lin}}$	$10^7\Omega_K^{\text{nl}}$
0.0	4.97	7.83
0.3	4.97	7.22
0.5	4.76	6.65
0.7	4.49	6.06
1.0	4.07	5.26
1.3	3.67	4.59
1.5	3.43	4.21

fluctuations into kinetic energy, most of which thermalizes via shocks. Due to energy conservation, we expect $\Omega_{\text{th}}/\Omega_W^{\text{ref}}$ to be of order unity but, importantly, it should not exceed unity. Verifying this property is an interesting test of our understanding of baryons and dark matter as these two quantities are obtained using fundamentally different estimates: Ω_W^{halo} is computed using the theoretical framework of the halo model which is driven by dark matter statistics, and Ω_{th} using observations of the SZ effect.

Our analysis shows that $\Omega_{\text{th}}/\Omega_W^{\text{ref}} \simeq 0.8$ at $z = 0$. It therefore provides an important check of our understanding of the related statistical properties of these quantities. Of particular interest, thanks to the enhanced accuracy of the Ω_{th} and Ω_W^{ref} estimates, we are now in a position to probe the amount of non-thermal pressure. Our analysis has allowed us to derive $\Omega_{\text{non-th}} \simeq 0.37 \times 10^{-8}$ at $z = 0$.

Now, what accounts for this? A promising candidate for non-thermal pressure quantified by $\Omega_{\text{non-th}}$ is the bulk and turbulent motion of gas sourced by mass accretion and structure formation (Dolag et al. 2005; Iapichino & Niemeyer 2008; Vazza et al. 2006, 2009, 2016, 2018; Lau et al. 2009; Maier et al. 2009; Shaw et al. 2010; Iapichino et al. 2011; Battaglia et al. 2012; Nelson et al. 2014a; Shi & Komatsu 2014; Shi et al. 2015; Angelinelli et al. 2020). An analytical model (Shi & Komatsu 2014) validated by cosmological hydrodynamical simulations (Shi et al. 2015) suggests the following picture: the non-thermal energy is sourced by the mass growth of halos via mergers and accretion, and dissipates with a time-scale determined by the turnover time of the largest turbulence eddies. The timescale of dissipation is on the order of the local dynamical time, which is shorter in the core and longer in the outskirts of halos. Thus, the fraction of the non-thermal energy relative to

the total increases with radii, reaching tens of percent at the virial radius depending on halo mass and redshift. Therefore, the amount of non-thermal energy in this form seems sufficient to account for the non-thermal pressure budget given in Eq. (25).

Our Ω_{th} measurement, as well as the inferred amount of non-thermal pressure or energy density, should add to the list of useful, non-trivial tests for modern cosmological hydrodynamical simulations of formation and evolution of galaxies and clusters of galaxies (Vogelsberger et al. 2014; Dubois et al. 2014; Le Brun et al. 2014; Schaye et al. 2015; Dolag et al. 2016; McCarthy et al. 2017; Pillepich et al. 2018). It would provide further insights to the balance of thermal and non-thermal energy budgets of large-scale structure of the Universe, which is related to the physical ingredients of galaxy formation such as the AGN feedback and hot/cold mode gas accretion onto halos (Kereš et al. 2005; Dekel et al. 2009).

Observational evidence for non-thermal motion in galaxy clusters and groups includes line broadening of metal lines in X-ray bands (Sunyaev et al. 2003; Inogamov & Sunyaev 2003; Hitomi Collaboration et al. 2016; Lau et al. 2017), the kinetic SZ effect (Sunyaev et al. 2003; Inogamov & Sunyaev 2003; Sayers et al. 2013, 2019; Adam et al. 2017) and surface brightness fluctuations in X-ray (Schuecker et al. 2004; Kawahara

et al. 2008; Churazov et al. 2012, 2016) as well as in the thermal SZ effect (Khatri & Gaspari 2016; Ueda et al. 2018; Di Mascolo et al. 2019). On-going and future high sensitivity, high spectral and spatial resolution X-ray (*eROSITA*, *XRISM*, *ATHENA*) and SZ experiments (Mroczkowski et al. 2019, for a review) as well as cross-correlation of the future large-scale survey data of the microwave sky from Simons Observatory (Ade et al. 2019) and CMB-S4 (Abazajian et al. 2016) with galaxy survey data (Battaglia et al. 2017; Pandey et al. 2020) would provide stringent tests of the thermal and non-thermal cosmic energy inventory.

ACKNOWLEDGMENTS

EK thanks N. Afshordi, B. Bolliet, B. M. Schäfer, D. Spergel, and V. Springel for useful comments on the draft. This work was supported in part by NSF grant AST1313302 and NASA grant NNX16AF64G (YC, BM), the Excellence Cluster ORIGINS which is funded by the Deutsche Forschungsgemeinschaft (DFG, German Research Foundation) under Germany's Excellence Strategy - EXC-2094 - 390783311 (EK), and JSPS KAKENHI Grant Number JP15H05896 (RM, EK) and JP20K14515 (RM). The Kavli IPMU is supported by World Premier International Research Center Initiative (WPI), MEXT, Japan.

REFERENCES

- Abazajian, K. N., Adshead, P., Ahmed, Z., et al. 2016, arXiv e-prints, arXiv:1610.02743
- Adam, R., Bartalucci, I., Pratt, G. W., et al. 2017, *A&A*, 598, A115
- Ade, P., Aguirre, J., Ahmed, Z., et al. 2019, *JCAP*, 2019, 056
- Angelinelli, M., Vazza, F., Giocoli, C., et al. 2020, *MNRAS*, 495, 864
- Ansarifard, S., Rasia, E., Biffi, V., et al. 2020, *A&A*, 634, A113
- Arnaud, M., Pratt, G. W., Piffaretti, R., et al. 2010, *A&A*, 517, A92
- Ata, M., Baumgarten, F., Bautista, J., et al. 2018, *MNRAS*, 473, 4773
- Battaglia, N., Bond, J. R., Pfrommer, C., & Sievers, J. L. 2012, *ApJ*, 758, 74
- Battaglia, N., Ferraro, S., Schaan, E., & Spergel, D. N. 2017, *JCAP*, 2017, 040
- Battaglia, N., Hill, J. C., & Murray, N. 2015, *ApJ*, 812, 154
- Bautista, J. E., Vargas-Magaña, M., Dawson, K. S., et al. 2018, *ApJ*, 863, 110
- Biffi, V., Borgani, S., Murante, G., et al. 2016, *ApJ*, 827, 112
- Blanton, M. R., Schlegel, D. J., Strauss, M. A., et al. 2005, *AJ*, 129, 2562
- Blas, D., Lesgourgues, J., & Tram, T. 2011, *JCAP*, 2011, 034
- Bocquet, S., Saro, A., Dolag, K., & Mohr, J. J. 2016, *MNRAS*, 456, 2361
- Bolliet, B., Brinckmann, T., Chluba, J., & Lesgourgues, J. 2020, *MNRAS*, 497, 1332
- Bolliet, B., Comis, B., Komatsu, E., & Macías-Pérez, J. F. 2018, *MNRAS*, 477, 4957
- Bryan, G. L. 2000, *ApJL*, 544, L1
- Bryan, G. L., & Norman, M. L. 1998, *ApJ*, 495, 80
- Castorina, E., Sefusatti, E., Sheth, R. K., Villaescusa-Navarro, F., & Viel, M. 2014, *JCAP*, 2014, 049
- Cen, R., & Ostriker, J. P. 1999, *ApJ*, 514, 1
- Chiang, Y.-K., Makiya, R., Ménard, B., & Komatsu, E. 2020, *ApJ*, 902, 56
- Churazov, E., Arevalo, P., Forman, W., et al. 2016, *MNRAS*, 463, 1057

- Churazov, E., Vikhlinin, A., Zhuravleva, I., et al. 2012, *MNRAS*, 421, 1123
- Cooray, A., & Sheth, R. 2002, *PhR*, 372, 1
- Costanzi, M., Villaescusa-Navarro, F., Viel, M., et al. 2013, *JCAP*, 2013, 012
- Crichton, D., Gralla, M. B., Hall, K., et al. 2016, *MNRAS*, 458, 1478
- Davis, M., Miller, A., & White, S. D. M. 1997, *ApJ*, 490, 63
- Dekel, A., Birnboim, Y., Engel, G., et al. 2009, *Nature*, 457, 451
- Di Mascolo, L., Churazov, E., & Mroczkowski, T. 2019, *MNRAS*, 487, 4037
- Dmitriev, N. A., & Zeldovich, Y. B. 1964, *Soviet Journal of Experimental and Theoretical Physics*, 18, 793
- Dolag, K., Komatsu, E., & Sunyaev, R. 2016, *MNRAS*, 463, 1797
- Dolag, K., Vazza, F., Brunetti, G., & Tormen, G. 2005, *MNRAS*, 364, 753
- Dubois, Y., Pichon, C., Welker, C., et al. 2014, *MNRAS*, 444, 1453
- Duffy, A. R., Schaye, J., Kay, S. T., & Dalla Vecchia, C. 2008, *MNRAS*, 390, L64
- Eisenstein, D. J., Annis, J., Gunn, J. E., et al. 2001, *AJ*, 122, 2267
- Fukugita, M., & Peebles, P. J. E. 2004, *ApJ*, 616, 643
- Gnedin, O. Y., Kravtsov, A. V., Klypin, A. A., & Nagai, D. 2004, *ApJ*, 616, 16
- Gonzalez, A. H., Sivanandam, S., Zabludoff, A. I., & Zaritsky, D. 2013, *ApJ*, 778, 14
- Greco, J. P., Hill, J. C., Spergel, D. N., & Battaglia, N. 2015, *ApJ*, 808, 151
- Hall, K. R., Zakamska, N. L., Addison, G. E., et al. 2019, *MNRAS*, 490, 2315
- Henson, M. A., Barnes, D. J., Kay, S. T., McCarthy, I. G., & Schaye, J. 2017, *MNRAS*, 465, 3361
- Hill, J. C., Baxter, E. J., Lidz, A., Greco, J. P., & Jain, B. 2018, *PhRvD*, 97, 083501
- Hill, J. C., & Spergel, D. N. 2014, *JCAP*, 2014, 030
- Hitomi Collaboration, Aharonian, F., Akamatsu, H., et al. 2016, *Nature*, 535, 117
- Hojjati, A., McCarthy, I. G., Harnois-Deraps, J., et al. 2015, *JCAP*, 2015, 047
- Hojjati, A., Tröster, T., Harnois-Déraps, J., et al. 2017, *MNRAS*, 471, 1565
- Horowitz, B., & Seljak, U. 2017, *MNRAS*, 469, 394
- Hurier, G., & Lacasa, F. 2017, *A&A*, 604, A71
- Iapichino, L., & Niemeyer, J. C. 2008, *MNRAS*, 388, 1089
- Iapichino, L., Schmidt, W., Niemeyer, J. C., & Merklein, J. 2011, *MNRAS*, 414, 2297
- Ichiki, K., & Takada, M. 2012, *PhRvD*, 85, 063521
- Inogamov, N. A., & Sunyaev, R. A. 2003, *Astronomy Letters*, 29, 791
- Irvine, W. M. 1961, PhD thesis, Harvard University
- Jeltema, T. E., Hallman, E. J., Burns, J. O., & Motl, P. M. 2008, *ApJ*, 681, 167
- Kawahara, H., Reese, E. D., Kitayama, T., Sasaki, S., & Suto, Y. 2008, *ApJ*, 687, 936
- Kay, S. T., Thomas, P. A., Jenkins, A., & Pearce, F. R. 2004, *MNRAS*, 355, 1091
- Kereš, D., Katz, N., Weinberg, D. H., & Davé, R. 2005, *MNRAS*, 363, 2
- Khatri, R., & Gaspari, M. 2016, *MNRAS*, 463, 655
- Komatsu, E., & Kitayama, T. 1999, *ApJL*, 526, L1
- Komatsu, E., & Seljak, U. 2001, *MNRAS*, 327, 1353
- . 2002, *MNRAS*, 336, 1256
- Koukoufilippas, N., Alonso, D., Bilicki, M., & Peacock, J. A. 2020, *MNRAS*, 491, 5464
- Lau, E. T., Gaspari, M., Nagai, D., & Coppi, P. 2017, *ApJ*, 849, 54
- Lau, E. T., Kravtsov, A. V., & Nagai, D. 2009, *ApJ*, 705, 1129
- Lau, E. T., Nagai, D., Avestruz, C., Nelson, K., & Vikhlinin, A. 2015, *ApJ*, 806, 68
- Layzer, D. 1963, *ApJ*, 138, 174
- Le Brun, A. M. C., McCarthy, I. G., Schaye, J., & Ponman, T. J. 2014, *MNRAS*, 441, 1270
- Lim, S. H., Mo, H. J., Li, R., et al. 2018a, *ApJ*, 854, 181
- Lim, S. H., Mo, H. J., Wang, H., & Yang, X. 2018b, *MNRAS*, 480, 4017
- Lynden-Bell, D. 1967, *MNRAS*, 136, 101
- Ma, Y.-Z., Van Waerbeke, L., Hinshaw, G., et al. 2015, *JCAP*, 2015, 046
- Maier, A., Iapichino, L., Schmidt, W., & Niemeyer, J. C. 2009, *ApJ*, 707, 40
- Makiya, R., Ando, S., & Komatsu, E. 2018, *MNRAS*, 480, 3928
- Makiya, R., Hikage, C., & Komatsu, E. 2020, *PASJ*, 72, 26
- McCarthy, I. G., Schaye, J., Bird, S., & Le Brun, A. M. C. 2017, *MNRAS*, 465, 2936
- Meneghetti, M., Rasia, E., Merten, J., et al. 2010, *A&A*, 514, A93
- Miniati, F., Ryu, D., Kang, H., et al. 2000, *ApJ*, 542, 608
- Miville-Deschênes, M.-A., & Lagache, G. 2005, *ApJS*, 157, 302
- Mroczkowski, T., Nagai, D., Basu, K., et al. 2019, *SSRv*, 215, 17
- Nagai, D., Vikhlinin, A., & Kravtsov, A. V. 2007, *ApJ*, 655, 98
- Navarro, J. F., Frenk, C. S., & White, S. D. M. 1996, *ApJ*, 462, 563

- . 1997, *ApJ*, 490, 493
- Nelson, K., Lau, E. T., & Nagai, D. 2014a, *ApJ*, 792, 25
- Nelson, K., Lau, E. T., Nagai, D., Rudd, D. H., & Yu, L. 2014b, *ApJ*, 782, 107
- Nelson, K., Rudd, D. H., Shaw, L., & Nagai, D. 2012, *ApJ*, 751, 121
- Osato, K., Flender, S., Nagai, D., Shirasaki, M., & Yoshida, N. 2018, *MNRAS*, 475, 532
- Osato, K., Shirasaki, M., Miyatake, H., et al. 2020, *MNRAS*, 492, 4780
- Pandey, S., Baxter, E. J., & Hill, J. C. 2020, *PhRvD*, 101, 043525
- Pandey, S., Baxter, E. J., Xu, Z., et al. 2019, *PhRvD*, 100, 063519
- Pâris, I., Petitjean, P., Ross, N. P., et al. 2017, *A&A*, 597, A79
- Peebles, P. J. E. 1980, *The large-scale structure of the universe* (Princeton University Press)
- Piffaretti, R., & Valdarnini, R. 2008, *A&A*, 491, 71
- Pillepich, A., Springel, V., Nelson, D., et al. 2018, *MNRAS*, 473, 4077
- Planck Collaboration, Ade, P. A. R., Aghanim, N., et al. 2013a, *A&A*, 557, A52
- . 2013b, *A&A*, 550, A131
- . 2014, *A&A*, 571, A20
- Planck Collaboration, Adam, R., Ade, P. A. R., et al. 2016a, *A&A*, 594, A8
- Planck Collaboration, Aghanim, N., Arnaud, M., et al. 2016b, *A&A*, 594, A22
- Planck Collaboration, Ade, P. A. R., Aghanim, N., et al. 2016c, *A&A*, 594, A24
- Planck Collaboration, Aghanim, N., Akrami, Y., et al. 2020, *A&A*, 641, A6
- Rasia, E., Ettori, S., Moscardini, L., et al. 2006, *MNRAS*, 369, 2013
- Rasia, E., Meneghetti, M., Martino, R., et al. 2012, *New Journal of Physics*, 14, 055018
- Refregier, A., Komatsu, E., Spergel, D. N., & Pen, U.-L. 2000, *PhRvD*, 61, 123001
- Reid, B., Ho, S., Padmanabhan, N., et al. 2016, *MNRAS*, 455, 1553
- Ruan, J. J., McQuinn, M., & Anderson, S. F. 2015, *ApJ*, 802, 135
- Salvati, L., Douspis, M., & Aghanim, N. 2018, *A&A*, 614, A13
- Salvati, L., Douspis, M., Ritz, A., Aghanim, N., & Babul, A. 2019, *A&A*, 626, A27
- Sayers, J., Mroczkowski, T., Zemcov, M., et al. 2013, *ApJ*, 778, 52
- Sayers, J., Montaña, A., Mroczkowski, T., et al. 2019, *ApJ*, 880, 45
- Schaan, E., Ferraro, S., Amodeo, S., et al. 2020, *arXiv e-prints*, arXiv:2009.05557
- Schaye, J., Crain, R. A., Bower, R. G., et al. 2015, *MNRAS*, 446, 521
- Schneider, D. P., Richards, G. T., Hall, P. B., et al. 2010, *AJ*, 139, 2360
- Schuecker, P., Finoguenov, A., Miniati, F., Böhringer, H., & Briel, U. G. 2004, *A&A*, 426, 387
- Scoccimarro, R., Sheth, R. K., Hui, L., & Jain, B. 2001, *ApJ*, 546, 20
- Seljak, U. 2000, *MNRAS*, 318, 203
- Shaw, L. D., Nagai, D., Bhattacharya, S., & Lau, E. T. 2010, *ApJ*, 725, 1452
- Shi, X. 2016, *MNRAS*, 461, 1804
- Shi, X., & Komatsu, E. 2014, *MNRAS*, 442, 521
- Shi, X., Komatsu, E., Nagai, D., & Lau, E. T. 2016, *MNRAS*, 455, 2936
- Shi, X., Komatsu, E., Nelson, K., & Nagai, D. 2015, *MNRAS*, 448, 1020
- Smith, R. E., Peacock, J. A., Jenkins, A., et al. 2003, *MNRAS*, 341, 1311
- Soergel, B., Giannantonio, T., Efstathiou, G., Puchwein, E., & Sijacki, D. 2017, *MNRAS*, 468, 577
- Spacek, A., Scannapieco, E., Cohen, S., Joshi, B., & Mauskopf, P. 2016, *ApJ*, 819, 128
- . 2017, *ApJ*, 834, 102
- Strauss, M. A., Weinberg, D. H., Lupton, R. H., et al. 2002, *AJ*, 124, 1810
- Sunyaev, R. A., Norman, M. L., & Bryan, G. L. 2003, *Astronomy Letters*, 29, 783
- Sunyaev, R. A., & Zeldovich, Y. B. 1972, *Comments on Astrophysics and Space Physics*, 4, 173
- Takahashi, R., Sato, M., Nishimichi, T., Taruya, A., & Oguri, M. 2012, *ApJ*, 761, 152
- Tanimura, H., Hinshaw, G., McCarthy, I. G., et al. 2020, *MNRAS*, 491, 2318
- Tinker, J., Kravtsov, A. V., Klypin, A., et al. 2008, *ApJ*, 688, 709
- Tinker, J. L., Robertson, B. E., Kravtsov, A. V., et al. 2010, *ApJ*, 724, 878
- Ueda, S., Kitayama, T., Oguri, M., et al. 2018, *ApJ*, 866, 48
- van Daalen, M. P., Schaye, J., Booth, C. M., & Dalla Vecchia, C. 2011, *MNRAS*, 415, 3649
- Van Waerbeke, L., Hinshaw, G., & Murray, N. 2014, *PhRvD*, 89, 023508
- Vazza, F., Angelinelli, M., Jones, T. W., et al. 2018, *MNRAS*, 481, L120

- Vazza, F., Brunetti, G., Kritsuk, A., et al. 2009, *A&A*, 504, 33
- Vazza, F., Tormen, G., Cassano, R., Brunetti, G., & Dolag, K. 2006, *MNRAS*, 369, L14
- Vazza, F., Wittor, D., Brüggem, M., & Gheller, C. 2016, *Galaxies*, 4, 60
- Vikram, V., Lidz, A., & Jain, B. 2017, *MNRAS*, 467, 2315
- Villaescusa-Navarro, F., Marulli, F., Viel, M., et al. 2014, *JCAP*, 2014, 011
- Vogelsberger, M., Genel, S., Springel, V., et al. 2014, *Nature*, 509, 177
- White, S. D. M. 1996, in *Gravitational dynamics*, ed. O. Lahav, E. Terlevich, & R. J. Terlevich, 121
- York, D. G., Adelman, J., Anderson, John E., J., et al. 2000, *AJ*, 120, 1579
- Zhang, C., Churazov, E., Dolag, K., Forman, W. R., & Zhuravleva, I. 2020, *MNRAS*, 494, 4539
- Zhang, P., & Pen, U.-L. 2001, *ApJ*, 549, 18
- Zhang, P., Pen, U.-L., & Trac, H. 2004, *MNRAS*, 355, 451